THE JOURNAL OF PHYSICAL CHEMISTRY C

Article

Cite This: J. Phys. Chem. C 2019, 123, 8785−8792

pubs.acs.org/JPCC

Identifying Reaction Species by Evolutionary Fitting and Kinetic Analysis: An Example of CO_2 Hydrogenation in DRIFTS

Kun Zhao,*[,†,∥,⊥] Ligang Wang,[‡,§,⊥] Emanuele Moioli,[†,∥] Marco Calizzi,*[,†,∥] and Andreas Züttel[†,∥]

[†]Laboratory of Materials for Renewable Energy, Institute of Chemical Sciences and Engineering, [‡]Group of Energy Materials, Institute of Mechanical Engineering, and [§]Industrial Process and Energy Systems Engineering, Institute of Mechanical Engineering, École Polytechnique Fédérale de Lausanne (EPFL), 1951 Sion, Switzerland

[∥]Swiss Federal Laboratories for Materials Science and Technology (EMPA), 8600 Dübendorf, Switzerland

Supporting Information

ABSTRACT: Diffuse reflectance infrared Fourier transform spectroscopy (DRIFTS) investigations of molecules at the surface of catalysts exhibit a strong overlap of the adsorption peaks. Therefore, the investigation of the CO_2 hydrogenation on a highly active catalyst surface requires a deconvolution of the adsorption spectra to clearly assign the signal to the chemical species. We developed an autonomous and efficient bi-level evolutionary Gaussian fitting (BEGF) procedure with a genetic algorithm at the upper level and a multipeak Gaussian fitting algorithm at the lower level to analyze self-consistently the set of spectra of an entire experiment. We show two examples of the application of BEGF procedure by analyzing the DRIFTS spectral sets of ex situ $HCOO^-$* and CO_2 hydrogenation on Ru/Al_2O_3. The fitting procedure deconvoluted the overlapped peaks and identified the bond vibrations of carbon monoxide, formate, bicarbonate, and carbonate through the developing trends of the peak intensities along the reaction. These revealed the progression of those species over the reaction timeline.

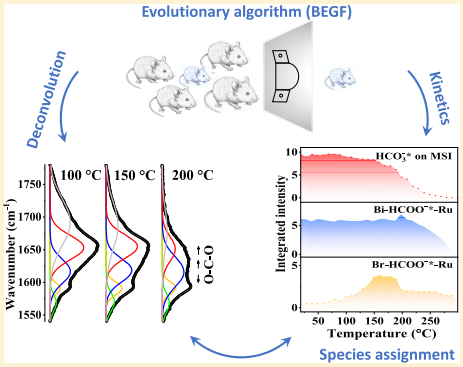

1. INTRODUCTION

Heterogeneous catalysis on surfaces, such as CO_2 hydrogenation catalysis, has been widely studied by diffuse reflectance infrared Fourier transform spectroscopy (DRIFTS), as both the gas-phase components and the surface adsorption species can be detected in situ and in operando.[1−7] The correct assignment of the infrared (IR) peaks is not easy because they are strongly overlapped. Especially, the O−C−O asymmetric stretching modes of HCO_3^-, $HCOO^-$, $COOH^-$, and bent $CO_2^{\delta-}$ share very close positions in the range of 1800−1300 cm^{-1}.[8] This has led to discrepant explanations of the production of the adsorption species, thence diverse reaction pathways about either bicarbonate, formate, or carbon monoxide is the key intermediate.[7,9−11] Many issues affect the analysis of CO_2 hydrogenation using IR spectroscopy. First, the determination of the IR peak positions of the species present on reactive surfaces such as Ru, Rh, Pd, etc. is not simple due to the strong overlap of the peaks. As a result, the manual assignment of the peak positions among the multipeaks and shoulders does not have an obvious unique solution. Second, some subpeaks in the overlapped region vanish or appear during the reaction, which is easily neglected in the analysis. Thus, assigning the peaks using data only at one or a few stages in the reaction can lose information. A global analysis of the spectra done over the entire course of the reaction is necessary. This brings us to the third issue: there is no efficient procedure to fit self-consistently the peaks of all of the spectra recorded during the reaction. Fitting spectra non-self-consistently, or using inconsistent parameters, can give an incorrect description of the development of the peaks along the reaction coordinate. A multipeak Gaussian curve fitting can be performed with nonlinear gradient-based solvers,[12] but the results depend strongly on the guesses of initial values and bounds of the parameters related to each peak. Bad guesses lead the solvers to be trapped at local optima, resulting in unsatisfactory or even wrong results.

Here, we tackle the three issues just raised by developing a novel bi-level evolutionary Gaussian fitting (BEGF) procedure to fit the peaks from a set of spectra and select the reasonably deconvoluted peaks automatically. This BEGF procedure combines gradient-free evolutionary algorithms at the upper level and nonlinear multipeak Gaussian fittings at the lower level to optimize the peaks. An evolutionary algorithm is an optimization algorithm that ranks the candidate solutions, recombines the parameters of the best ones to create a new generation of candidate solutions, and iterates till convergence is reached.[13] The evolutionary algorithm overcomes the problem of Gaussian fitting being trapped at local optima. The fitting results elucidate the developing trends of the resolved peaks along the reaction. According to the similarities of the peak developments in the reaction, and combined with the peak positions from the standard samples such as formic

Received: November 15, 2018
Revised: February 27, 2019
Published: March 11, 2019

DOI: 10.1021/acs.jpcc.8b11105
J. Phys. Chem. C 2019, 123, 8785−8792

acid (HCOOH), sodium carbonate (Na_2CO_3), calcium carbonate ($CaCO_3$), sodium bicarbonate ($NaHCO_3$), and potassium bicarbonate ($KHCO_3$), the peaks were clearly assigned to the bond vibrations of the specific species.

In the next section, we provide a description of the BEGF algorithm. More detailed information and the MATLAB code used for the work reported here are given in the Supporting Information (SI). Later on, we describe the procedure with two examples: (1) formate hydrogenation where formate was from an HCOOH droplet and therefore named as ex situ $HCOO^{-}$* to distinguish the formate formed from the CO_2 hydrogenation process; (2) CO_2 hydrogenation. These two examples show how the procedure helps the assignment of the peaks and analyze the reactive progression of the reaction species.

2. FITTING AND EXPERIMENTAL METHODS

2.1. Bi-Level Evolutionary Gaussian Fitting (BEGF) Procedure. The multipeak Gaussian fitting is a least-square problem (eq 1a), which minimizes the sum of squared errors between the fitted value and the experimental data of the spectrum to find the best fit

$$\min_{\mathbf{a},\mathbf{b},\mathbf{c}} f = \sum_{i=1}^{N_s} \left(\sum_{j=W_s}^{W_e} (Y_{i,j}(\mathbf{a}_i, \mathbf{b}, \mathbf{c}_i) - Y_{i,j}^*)^2 \right),$$
$$\mathbf{a}_i = \{\dots a_{i,k} \dots\}, \mathbf{b} = \{\dots b_k \dots\}, \mathbf{c}_i = \{\dots c_{i,k} \dots\} \quad (1a)$$

with

$$Y_{i,j} = \sum_{k=1}^{N_{peak}} a_{i,k}\, e^{-(x-b_k/c_{i,k})^2} \quad (1b)$$

where i stands for the ith spectrum in the total N_s spectra and j is the wavenumber within the defined range $[W_s, W_e]$, where W_s and W_e are the starting and ending wavenumbers, respectively. $Y_{i,j}$ and $Y_{i,j}^*$ are the fitted and measured values, respectively. The variables $a_{i,k}$, b_k, and $c_{i,k}$ are the height, position, and width, respectively, of each Gaussian peak k ($1 \le k \le N_{peak}$). a_i and c_i vary along the reaction, whereas b is generally assumed not to change as the reaction proceeds.

The optimization problem is highly nonlinear due to the Gaussian function used in the definition of $Y_{i,j}$ (eq 1b). The whole problem can be solved by gradient-based solvers. However, in our experience with fitting DRIFTS spectra, gradient-based solvers get trapped at local minima depending on the guesses of the initial values of Gaussian parameters, and these guesses are usually obtained manually by time-consuming trial-and-error.

To overcome this difficulty, we decomposed the mathematical optimization problem into two levels: for the upper level, we used a genetic algorithm to provide initial values for a multipeak Gaussian fitting algorithm used on the lower level.

The scheme of the BEGF process is shown in Figure 1, with the problem decomposition described as follows:

Upper level

$$\min_{\mathbf{I},\mathbf{L},\mathbf{U}} \sum_{i=1}^{N_s} \delta_i(\mathbf{I}, \mathbf{L}, \mathbf{U}), \mathbf{I} = \{\dots\{I_{a_k}, I_{b_k}, I_{c_k}\}\dots\},$$
$$\mathbf{L} = \{\dots\{L_{a_k}, L_{b_k}, L_{c_k}\}\dots\}, \mathbf{U} = \{\dots\{U_{a_k}, U_{b_k}, U_{c_k}\}\dots\} \quad (2)$$

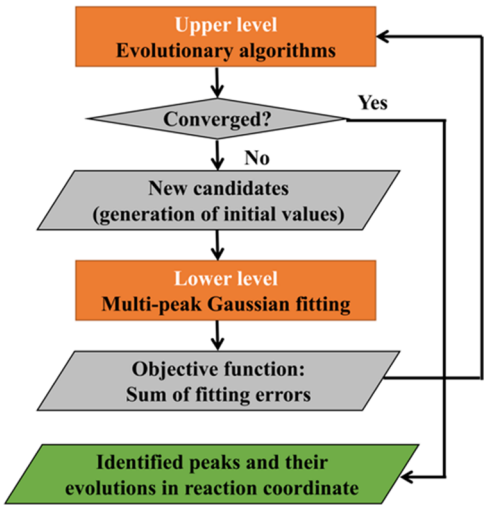

Figure 1. Developed bi-level evolutionary Gaussian fitting algorithm.

Lower level

$$\min_{\mathbf{a},\mathbf{b},\mathbf{c}} \delta_i(\mathbf{a}_i, \mathbf{b}, \mathbf{c}_i) = \min_{\mathbf{a},\mathbf{b},\mathbf{c}} \sum_{j=W_s}^{W_e} (Y_{i,j} - Y_{i,j}^*)^2$$
$$= \min_{\mathbf{a},\mathbf{b},\mathbf{c}} \sum_{j=W_s}^{W_e} \left(\sum_{k=1}^{N_{peak}} (a_{i,k}\, e^{-(x-b_k/c_{i,k})^2}) - Y_{i,j}^* \right)^2,$$
$$\mathbf{a}_i = \{\dots a_{i,k} \dots\}, \mathbf{b} = \{\dots b_k \dots\}, \mathbf{c}_i = \{\dots c_{i,k} \dots\} \text{ subject to}$$
$$L_{a_k} \le a_{i,k} \le U_{a_k}, L_{b_k} \le b_k \le U_{b_k}, L_{c_k} \le c_{i,k} \le U_{c_k} \quad (3)$$

where $\boldsymbol{I}$ shows the initial values of the parameters (a height, b position, and c width) of the Gaussian peaks. $\boldsymbol{L}$ and $\boldsymbol{U}$ are the lower and upper bounds of the parameters of the Gaussian peaks, respectively, which are used to constrain the multipeak Gaussian fitting.

The BEGF algorithm works as follows and is sketched in Figure 1. The original spectra are first corrected by subtracting a baseline, which was taken as a straight line between the end points of the defined wavenumber range. The baseline-corrected spectra are used in each run of the low-level algorithm. The solving procedure starts from the upper-level algorithm by generating a number of global candidate solutions [individuals, represented by a set of values of $\boldsymbol{I}$, $\boldsymbol{L}$, and $\boldsymbol{U}$ (eq 2), which are randomly generated within the user-specified bounds] to form an initial population. Each individual of the population is passed to the lower-level algorithm to obtain the best fit values for the parameters $\boldsymbol{a}_i$, $\boldsymbol{b}$, and $\boldsymbol{c}_i$ and to assign the sum of the fitting errors as the value of the objective function (eq 3). The evaluated individual is then passed back to the upper-level algorithm. After evaluating all individuals in the initial population, the upper-level algorithm compares the individuals and discards those with large errors. Afterward, the population starts to evolve iteratively by selecting some existing individuals as parents and generating a new individual as a child with certain crossover and mutation mechanisms. The newly generated child individual is further evaluated in the lower level, returned to the upper level with the objective value, and compared with the parent individuals. The child individual will be preserved if better than the parents, otherwise discarded. In such a way, the whole population is updated by always keeping the better individuals until convergence is reached: no better individual is found after a

DOI: 10.1021/acs.jpcc.8b11105
J. Phys. Chem. C 2019, 123, 8785−8792

number of latest individual evaluations. The rate of convergence depends on the complexity of the spectra.

The BEGF algorithm starts with a user-specified number of Gaussian peaks. The redundant Gaussian peaks are removed when the L_{a_k} and U_{a_k} for peak k optimized at the upper level reach zero simultaneously.

Although good initial guesses are not needed for the genetic algorithm, using apparent information of the peaks in the spectra as initial values reduces the search time. Further details of the algorithm, including a MATLAB code implementation, are given in the SI.

Our bi-level algorithm is distinguished from available fitting codes by the following features: (1) It consistently fits the peaks in a given range of wavelengths across the entire set of spectra measured during a reaction; (2) the number of Gaussian peaks used for fitting is determined automatically; (3) the centroid of a given peak is identical for all spectra; (4) peak evolution directly gives the kinetics of the species; (5) manual intervention is not needed; and (6) good initial guesses are not necessary.

2.2. Experimental Methods. Ex situ $HCOO^-$* and CO_2 hydrogenation on Ru/Al_2O_3 (Sigma-Aldrich, 0.5 wt % loading on 3.2 mm pellets of Al_2O_3) pellets and Al_2O_3 (Sigma-Aldrich) pellets were carried out in the reaction chamber (HVC, Harrick Scientific) of DRIFTS (Bruker Tensor 27).

Ex situ $HCOO^-$* was obtained by adding one drop of formic acid onto the surface of Ru/Al_2O_3 or Al_2O_3 exposed to air, followed by pumping for 24 h to reach a vacuum of 5×10^{-3} mbar at room temperature (RT) in DRIFTS. The hydrogenation of HCOOH on Ru/Al_2O_3 and Al_2O_3 was performed by heating in 1 bar H_2 from RT to 350 °C at a rate of 1 °C/min in DRIFTS.

CO_2 hydrogenation was performed by mixing 200 mbar of CO_2 and 800 mbar of H_2 at RT and heating to 300 °C at a rate of 1 °C/min on H_2-pretreated Ru/Al_2O_3 and Al_2O_3 in DRIFTS, as in our previous work.[14]

3. RESULTS AND DISCUSSION

Ex situ $HCOO^-$* and CO_2 hydrogenations were used as reaction models for showing the complex spectra and how the BEGF program resolves the peak positions and variations. Formate is one of the intermediates of CO_2 hydrogenation. For this reason, we first analyzed the spectra of HCOOH hydrogenation to understand the reactivities of ex situ formate (ex situ $HCOO^-$*) in H_2 thermal reduction and then turned to the analysis of CO_2 hydrogenation.

3.1. BEGF Analysis of the Spectra of Ex Situ $HCOO^-$* Hydrogenation. *3.1.1. Convergence of Fitting.* The error evolution approaching convergence as a function of time and iteration numbers is illustrated in Figure 2a for the fitting in the range of 1800−1500 cm^{-1} from 20 to 220 °C, noting that above 220 °C the peaks and the baseline in this range changed significantly. Re-confining the range of the spectra above 220 °C for the new baseline correction is not necessary but is helpful in shortening the entire fitting time. We compared the fitting with coarse initial values from wide bounds and with fine initial values from readings of the spectra. Around 4 h were taken for the coarse initial values to reach convergence, with around 4000 iterations, and around 1 h for the convergence of fine initial values, with around 3000 iterations. The average time of iteration in Figure 2b decreased during evolution because the improved guesses (i.e., ***I***, ***L***, and ***U***) in the iteration

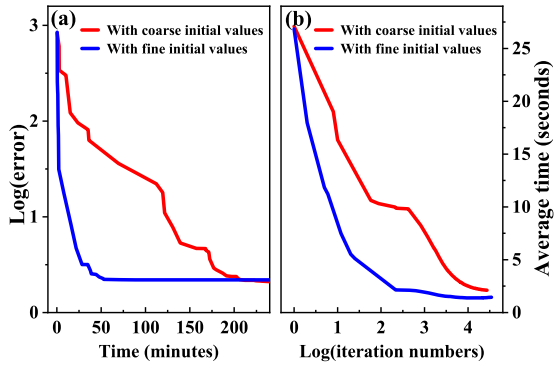

Figure 2. (a) Error evolution approaching convergence as a function of time and (b) average time of iteration for the fitting in the range of 1800−1500 cm^{-1} from 20 to 220 °C by BEGF.

reduced the time for each run of lower-level Gaussian fitting. Especially, with fine bounds of ***I***, ***L***, and ***U*** (blue line), the average time of iteration was shorter in the beginning due to the better solutions from the good bounds, which was beneficial in generating even better initial values for the next iteration. After enough iterations, the competitiveness of the preserved solutions for both blue and red lines became similar, as shown by the similarly converging average time after around 4000 iterations in Figure 2b.

3.1.2. Assignment of Adsorption Species Based on the Kinetic Results. The fitted spectra at 100, 150, 200, and 250 °C are shown in Figure 3a. Although the peaks are discernible, the evolution of the peak intensities along the reaction is not easily understandable by first sight of the spectra. We then used the BEGF program to produce the integrated intensities of each peak throughout the spectral set so that we obtained the evolution profile of each peak as a function of temperature. The intensity progression both facilitated the assignments of the peaks to specific species and revealed the reactivity of each species during the catalytic reaction.

As shown in Figure 3b,c, O−C−O asymmetric stretching (1560 and 1618 cm^{-1}; the assignments refer to Section S1.1 in SI) decreased from 200 °C until full reduction at 250 °C. The unassigned peaks at 1415 and 1405 cm^{-1} showed the same trend as O−C−O asymmetric stretching. By comparing that the relative intensity of the peak 1415 cm^{-1} to the peak 1405 cm^{-1} had a much stronger intensity on Al_2O_3 than on Ru/Al_2O_3 (Figure 3b,c and Figure S2a−c), the peak 1415 cm^{-1} was associated with the peak 1560 and 1405 cm^{-1} was associated with 1618 cm^{-1}. Since 1560 cm^{-1} had been paired with 1360 cm^{-1} as O−C−O asymmetric and symmetric stretchings on Al_2O_3 (Section S1.2 in SI), 1415 cm^{-1} could be assigned to C−H bending to complete the vibration modes of this species. Thence, the peak at 1405 cm^{-1} could be either C−H bending or O−C−O symmetric stretching, associated with the peak at 1618 cm^{-1}. The remaining three peaks at 1592, 1390, and 1375 cm^{-1} varied in the same trend (Figure 3d). In view that 1592 cm^{-1} was in the region of O−C−O asymmetric stretching, and was absent on Al_2O_3 under all experimental conditions (Figures S1 and S2), we assigned this peak to the O−C−O asymmetric stretching of formate on Ru sites. The other two peaks at 1390 and 1375 cm^{-1} were assigned to the C−H bending and O−C−O symmetric stretching, respectively, of this structure of formate. These assignments are consistent with the reported values.[1,7] The combinational vibration of C−H bending and O−C−O asymmetric

DOI: 10.1021/acs.jpcc.8b11105
J. Phys. Chem. C 2019, 123, 8785−8792

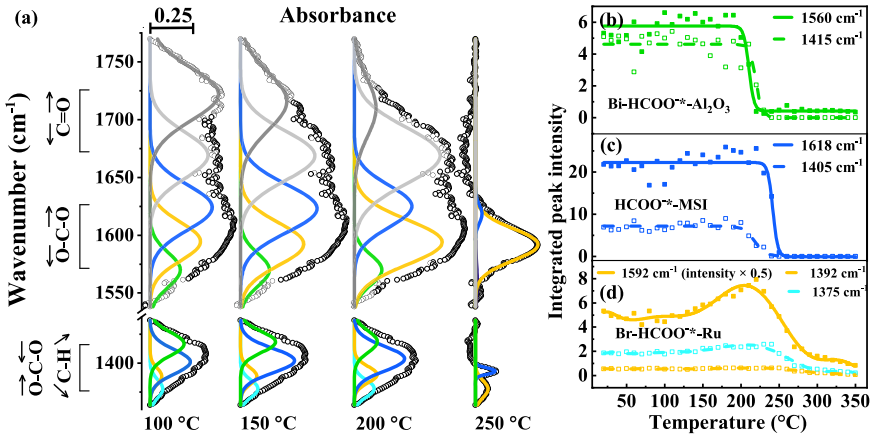

Figure 3. (a) Experimental spectra of ex situ $HCOO^-$* hydrogenation on Ru/Al_2O_3 (black circles) with fitted peaks (colored lines) in the ranges of 1770−1538 and 1440−1360 cm^{-1}. The fitting result of the evolution of (b) Bi-$HCOO^-$*-Al_2O_3, (c) $HCOO^-$*-MSI, and (d) Br-$HCOO^-$*-Ru during the reaction of ex situ $HCOO^-$* hydrogenation.

Table 1. Vibrational Modes and Infrared Peak Positions (cm^{-1}) of Formate, Bicarbonate, and Carbonate from CO_2 Hydrogenation[a]

species	C−H as. str.	C−H b.	C═O str.	O−C−O as. str.	O−C−O s. str.	O−H b.
HCOOH	2940 (cbn), 2871, 2760 (cbn)	1415, 1405	1748, 1670	1618, 1560	1405?, 1360	1220
$HCOO^-$*-MSI		1405	1720	1618	1405?	1220
Br-$HCOO^-$*-Ru	2896	1390		1592	1375	1220
Bi-$HCOO^-$*-Al_2O_3		1415	1710	1560	1360	1230
HCO_3^-*			1690	1650	1440	1230
CO_3^{2-}*			1500	1450		

[a]as. str.: asymmetric stretching; s. str: symmetric stretching; b.: bending; (cbn): combination modes; *: adsorbed state.

stretching at 2912 cm^{-1}, which gradually red-shifted to 2896 cm^{-1} during the reaction, also varied similarly as 1592 cm^{-1} (Figure S3). Thus, the peak at 2896 cm^{-1} could be classified as C−H stretching and a companion of the peak at 1592 cm^{-1}.

The splitting value between the asymmetric and symmetric stretchings ($\Delta\nu = \nu_{as} - \nu_s$) of O−C−O of $HCOO^-$* also indicates the orientations of the adsorption. For free and bridged formate, $\Delta\nu$ = 220−280 cm^{-1}. When $\Delta\nu$ is smaller than 220 cm^{-1}, formate is a bidentate structure; when $\Delta\nu$ is larger than 280 cm^{-1}, formate is a monodentate structure.[15] Therefore, formate with the O−C−O asymmetric stretching and symmetric stretching at 1592 and 1375 cm^{-1}, respectively, is in bridged orientation; formate with the O−C−O symmetric stretching at 1560 and 1360 cm^{-1} is in bidentate orientation. As has been explained above, formates with main peaks at 1592 and 1560 cm^{-1} are on Ru and Al_2O_3 sites, respectively; these two formates are abbreviated as Br-$HCOO^-$*-Ru and Bi-$HCOO^-$*-Al_2O_3, respectively. Formate with the main peak at 1618 cm^{-1} is located at the metal−support interface (MSI) because of its enhanced intensity on Ru/Al_2O_3 compared to that on Al_2O_3 (Section S1.1 in SI) and is thus named $HCOO^-$*-MSI. The related vibrational modes are listed in Table 1.

3.1.3. Reactivity of the Adsorption Species during Ex Situ $HCOO^-$ Hydrogenation.* The reactive trends of each species were exposed at the same time of fitting as shown in Figure 3b−d. Ex situ $HCOO^-$* on Ru/Al_2O_3 was reduced by H_2 at 200 °C until being fully consumed at 250 °C. Along with the decrease of ex situ $HCOO^-$*, three species emerged (Figures S3 and S4). Those were adsorbed carbon monoxide (CO*) on Ru, gaseous CO_2, and CH_4 gas with peaks in the ranges of 2100−1900, 2450−2250, and 3100−2900 cm^{-1}, respectively. Consequently, ex situ $HCOO^-$* on Ru/Al_2O_3 was reduced by H_2 at 200 °C until being fully consumed at 250 °C. The products were adsorbed CO*, gaseous CO_2, and gaseous CH_4. CO* came either from CO_2 reduction or from formate decomposition because CO* increased at the same temperature as CO_2 formation and kept increasing until 230 °C, whereas both CO_2 and formate were reduced. CH_4 also came either from formate or from CO_2 hydrogenation because CH_4 increased from 220 to 250 °C, whereas both formate and CO_2 reduced between 200 and 250 °C. There was no evidence of conversion between CO* and CH_4 because the concentrations of both CO* and CH_4 did not change above 270 °C.

In comparison, ex situ $HCOO^-$* hydrogenation on Al_2O_3 produced noticeable gaseous CO above 200 °C, which was represented by the occurrence of the rotational-vibrational peaks centered at 2142 cm^{-1} (Figure S2e), and invariant adsorbed CO_2*, which was represented by O═C═O symmetric stretching and resonance at 1387 and 1288 cm^{-1}, respectively (Figure S2f).

3.2. BEGF Analysis of the Spectra of CO_2 Hydrogenation. *3.2.1. Convergence of Fitting.* The information of the adsorption species during CO_2 hydrogenation on Ru/Al_2O_3 was mainly in the overlapped peaks below 2100 cm^{-1}, including HCO_3^-*, CO_3^{2-}*, $HCOO^-$*, and CO*, as we presented in our previous work.[14] The main contribution of this work is the methodology of decoupling the peaks and understanding their meaning via the BEGF program. The initial values of peak positions in BEGF were taken from the IR bands of the samples of carbonates and bicarbonates (Figure S5). Even though the initial values can also be used in regular multipeak Gaussian fitting procedures, the pseudosolutions from the local optima require the heavy manual work of

DOI: 10.1021/acs.jpcc.8b11105
J. Phys. Chem. C 2019, 123, 8785−8792

repeatedly adjusting the initial values to reach consistent results, including the number of Gaussian peaks, peak positions, and the variations of the integrated intensity for the related experiments. With the BEGF program, the spectral set of CO_2 hydrogenation was resolved by global solution within one day (Figure S6), and the fitted results are consistent with the results of our previous publication, obtained by an inefficient Gaussian fitting.

3.2.2. Assignment of Adsorption Species Based on the Kinetic Results. By comparing the trend of the integrated intensity of each peak along with the reaction coordinate (details in the following paragraphs), we found several groups of peaks in the wavenumber range of 1800−1480 cm^{-1} (Figure 4): group I: 1560 and 1360 cm^{-1}; group II: 1618 and 1405

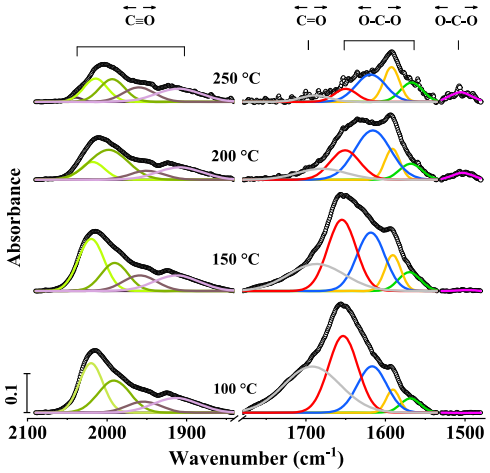

Figure 4. Spectra of CO_2 hydrogenation on Ru/Al_2O_3 (black circles) with fitted Gaussian peaks (colored lines) in the ranges of 2100−1840, 1780−1535, and 1530−1480 cm^{-1}. The vibrations in the range of 2100−1840 cm^{-1} are C≡O asymmetric stretching and in 1780−1535 cm^{-1} are the O−C−O asymmetric stretching of Bi-$HCOO^-$*-Al_2O_3 (green peak), $HCOO^-$*-MSI (blue peak), Br-$HCOO^-$*-Ru (yellow peak), HCO_3^-* (red peak), and CO_3^{2-}* (magenta).

cm^{-1}; group III: 2895, 1592, 1390, and 1375 cm^{-1}; group IV: 1650, 1440, and 1230 cm^{-1}; and group V: 1500 and 1460 cm^{-1}. Based on the assignment of formate from Section 3.1 (see also Table 1), groups I to III belonged to Br-$HCOO^-$*-Ru, $HCOO^-$*-MSI, and Bi-$HCOO^-$*-Al_2O_3, respectively. Referring to the measured peaks from the reference samples (Figure S5), groups IV and V belonged to adsorbed bicarbonate (HCO_3^-*) and adsorbed carbonate (CO_3^{2-}*), respectively. The splitting value of the O−C−O asymmetric (ν_{as}) and symmetric (ν_s) stretching bands of CO_3^{2-}* corresponds to different adsorption orientations. A splitting value ($\Delta\nu = \nu_{as} - \nu_s$) less than 100 cm^{-1} relates to a monodentate structure, $\Delta\nu$ larger than 200 cm^{-1} relates to a bidentate structure, and $\Delta\nu$ larger than 300 cm^{-1} relates to a bridged structure.[8] Since $\Delta\nu$ was far less than 100 cm^{-1} in our case, CO_3^{2-}* must be adsorbed on the surface with a monodentate structure. Its precursor HCO_3^-*, which has a similar molecular structure, could also be monodentate.

In the wavenumber range of 2100−1800 cm^{-1}, five adsorption structures of CO* were deconvoluted with peaks at 2035, 2015, 1990, 1950, and 1905 cm^{-1}. The high frequency at 2035 cm^{-1} was assigned to linear CO* on Ru^0; the peak at 2015 cm^{-1} was assigned to linear CO* on isolated Ru^0 surrounded by partially oxidized $Ru^{\delta+}$; the low frequencies at 1990, 1950, and 1905 cm^{-1} corresponded to bridged CO*.[7,12,17]

3.2.2.1. Isotope Spectra. To assist the peak assignment, especially to separate the strongly overlapped frequencies of O−C−O symmetric stretching and C−H bending modes, we have done the isotopic experiments with $^{13}CO_2$ at the same conditions as CO_2 hydrogenation. As shown in Figure 5a,b, there are certain shifts to the low frequency of the assigned peaks compared to the rich carbon species, including the shift of the C−H stretching of CH_4 from 3016 to 3007 cm^{-1}, the shift of the C−H bending of CH_4 from 1306 to 1297 cm^{-1}, and the shift of the center of the O═C═O asymmetric stretching of CO_2 from 2350 to 2283 cm^{-1}. The rest of the peak positions of the adsorption species are listed in Table 2. ^{13}C spectra facilitated to confirm the strong peaks of asymmetric stretching modes. However, it did not help the separation of O−C−O symmetric stretching and C−H bending modes. This could be understood that ^{13}C shifted the O−C−O symmetric stretching and C−H bending modes simultaneously as they both contain carbon bonds. Moreover, the signal/noise ratio did not improve as the intensity of infrared absorbance decreased due to the heavier mass.

Instead of using ^{13}C, we considered that D_2 could be more helpful to separate O−C−O and C−H vibrations. Because C−H would be changed to C−D, the vibrational frequency could be moved away from O−C−O vibrational frequency in the infrared spectra. Therefore, we did CO_2 deuteration by mixing 200 mbar CO_2 and 800 mbar pure D_2 using the same conditions and procedures. Unfortunately, the peak intensities were weakened more significantly in the low-frequency region (<1500 cm^{-1}) (Figure 5c,d). Except for the obvious peaks from CD_xH_{4-x} (x = 2, 3, 4),[16] only slight shifts of the strong peaks of the adsorption species were observed (Table 3).

Moreover, the reaction kinetics of these two isotopic experiments did not fully match the CO_2 hydrogenation results. For instance, the onset and ending temperatures of methane production are higher and lower, respectively, compared to those in the CO_2 hydrogenation experiment; the peak intensities were plausibly monotonically increasing/decreasing, nevertheless in fact occurring complicated shifts at high temperature (>150 °C). The similar phenomena were observed in the spectra of $^{13}CO_2$ hydrogenation in DRIFTS in ref 1. An investigation of the isotopic effect and comprehensive analysis of the kinetics from these isotopic data await future work to qualify the conclusions.

3.2.3. Reactivities of Adsorption Species during CO_2 Hydrogenation. 3.2.3.1. In Situ $HCOO^-$.* To distinguish the formate from the ex situ $HCOO^-$* in Section 3.1, we named the formate formed from the CO_2 hydrogenation process as in situ $HCOO^-$*. Bi-$HCOO^-$*-Al_2O_3 increased very slightly during the whole reaction (Figure 6a), indicating an inactive property. $HCOO^-$*-MSI was abundant and stable at up to 220 °C, after which it was consumed until its disappearance at 300 °C (Figure 6b), consistent with the result of the conversion equilibrium between $HCOO^-$*-MSI and CO_2^-* (Section S2.1 in SI). Conversely, Br-$HCOO^-$*-Ru increased from 70 to 150 °C, followed by a slow decrease (Figure 6c), implying multiple kinetic steps.

These in situ $HCOO^-$* species exhibited reactivities different from those of ex situ $HCOO^-$* species in the hydrogenation reaction. For in situ $HCOO^-$*, Bi-$HCOO^-$*-Al_2O_3 was inert, $HCOO^-$*-MSI was the most reactive species

DOI: 10.1021/acs.jpcc.8b11105
J. Phys. Chem. C 2019, 123, 8785−8792

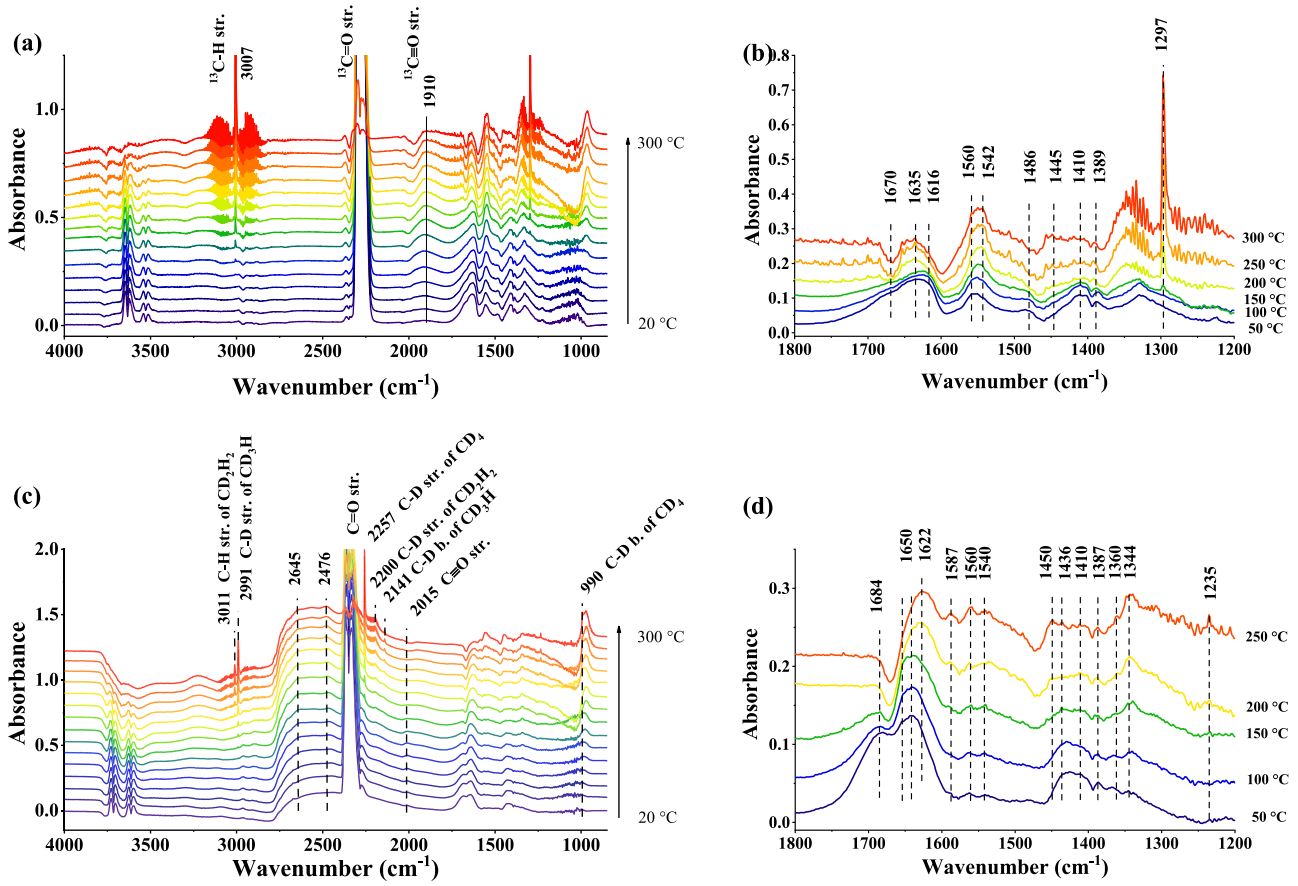

Figure 5. Full infrared spectra of (a) $^{13}CO_2$ hydrogenation by mixing 200 mbar $^{13}CO_2$ and 800 mbar H_2, after heating from 20 to 300 °C at 1 °C/min, (c) CO_2 deuteration in pure D_2 by mixing 200 mbar CO_2 and 800 mbar D_2, after heating from 20 to 300 °C at 1 °C/min. The extracted spectra in the wavenumber range between 1800 and 1200 cm^{-1} from (b) $^{13}CO_2$ hydrogenation and (d) CO_2 deuteration.

Table 2. Vibrational Modes and Infrared Peak Positions (cm^{-1}) of ^{13}C-Formate, -Bicarbonate, and -Carbonate from $^{13}CO_2$ Hydrogenation

species	^{13}C═O str.	O−^{13}C−O as. str.	O−^{13}C−O s. str.	O−H b.
H^{13}COO$^-$*-MSI	1700	1616		1220
Br-H^{13}COO$^-$*-Ru		1575		
Bi-H^{13}COO$^-$*-Al_2O_3				
H$^{13}CO_3^-$*	1670	1635		1230

Table 3. Vibrational Modes and Infrared Peak Positions (cm^{-1}) of D-Formate, -Bicarbonate, and -Carbonate from CO_2 Hydrogenation in Pure D_2[a]

species	C═O str.	O−C−O as. str.	O−C−O s. str.	O−D b.
DCOO$^-$*-MSI	1705	1622	1410	
Br-DCOO$^-$*-Ru		1587		
Bi-DCOO$^-$*-Al_2O_3		1560		
DCO_3^-*	1684	1659	1436	1230
CO_3^{2-}*		1500	1450	

[a]Note: carbon not labeled is regular ^{12}C.

toward reduction, and Br-HCOO$^-$*-Ru was formed during the reaction until 150 °C and was then consumed. For ex situ HCOO$^-$*, Bi-HCOO$^-$*-Al_2O_3 and HCOO$^-$*-MSI were the most reactive species toward reduction and Br-HCOO$^-$*-Ru increased between 100 and 220 °C, followed by a decrease.

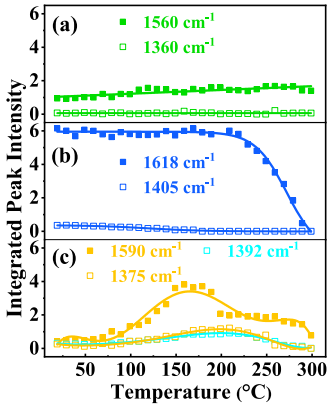

Figure 6. Fitting result of the evolution of (a) Bi-HCOO$^-$*-Al_2O_3, (b) HCOO$^-$*-MSI, and (c) Br-HCOO$^-$*-Ru during the CO_2 hydrogenation.

Therefore, the ex situ HCOO$^-$* assists in the peak assignments for in situ HCOO$^-$* but not in the prediction of the reactivities of the species.

3.2.3.2. HCO_3^- and CO_3^{2-}*.* HCO_3^-* on Ru/Al_2O_3 decreased slowly below 130 °C and then accelerated until complete consumption at 300 °C (Figure 7a). In comparison, HCO_3^-* on Al_2O_3 was reduced at 100 °C and fully converted at 160 °C (Figure S7a,b). This illustrated that HCO_3^-* was formed continuously on Ru/Al_2O_3 from CO_2 until the CO_2 concentration dropped but could not be continuously formed

DOI: 10.1021/acs.jpcc.8b11105
J. Phys. Chem. C 2019, 123, 8785−8792

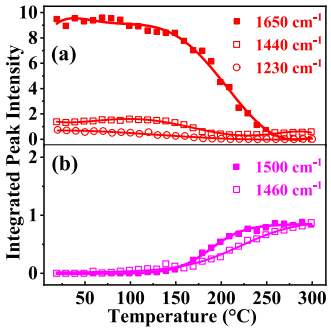

Figure 7. Fitting result of the evolution of (a) HCO_3^-* and (b) CO_3^{2-}* during CO_2 hydrogenation.

on Al_2O_3. In addition, the peak intensity of HCO_3^-* was much stronger on Ru/Al_2O_3 than on Al_2O_3. These implied that HCO_3^-* on Ru/Al_2O_3 was formed at the MSI. HCO_3^-* reduction showed a relation with CO_3^{2-}* formation above 200 °C (Figure 7b), indicating a deprotonation process.

*3.2.3.3. CO**. Five CO* on Ru/Al_2O_3 showed distinct reactivities. The linear CO* on Ru^0 was of negligible intensity and invariable, whereas the linear CO* on isolated Ru^0 showed an accumulation till 150 °C and a consumption afterward (Figure 8a). The bridged CO* exhibited an increase until 100

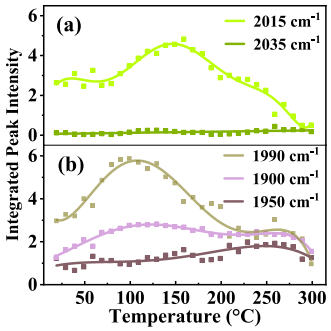

Figure 8. Fitting result of the evolution of (a) linear CO* and (b) bridged CO* during the reaction.

°C, followed by a decrease until reaching an equilibrium level at 200 °C (Figure 8b). These plots suggested that linear CO* on Ru^0 was inactive in CO_2 hydrogenation reaction. The other four forms of CO* participate in the reaction, yet carrying distinct reactivities. It has been reported that the different peak position of CO* is the result of the changed coverage of CO*.[9,17] The peak red-shifted when CO* coverage increased. This happened by supplying low-pressure CO gas to single-crystalline metal surfaces at a certain low temperature.[18] However, in our reaction conditions, the broad CO* peak showed the evolution of subpeaks related to the kinetics of each adsorption structure of CO* during the reaction. Among those structures of CO*, linear CO* on isolated Ru^0, surrounded by partially oxidized $Ru^{\delta+}$, showed a longer accumulation and a faster reduction, indicating a higher reactivity than the other structures of CO*.

On the other hand, CO* on Al_2O_3 generated one broad and weak peak between 2200 and 2100 cm^{-1}. This peak disappeared after pumping to a vacuum (Figure S10), in accordance with results reported for adsorbed CO* on metal oxides from CO gas.[19] The weak adsorption and high frequency (>2100 cm^{-1}) of CO* on Al_2O_3 confirmed the strong adsorption and low frequency (<2100 cm^{-1}) of CO* on Ru/Al_2O_3 adsorbed on Ru sites.

4. CONCLUSIONS

We resolved comprehensively the strongly overlapped and controversial IR peaks of CO_2 hydrogenation reaction in DRIFTS by a bi-level evolutionary Gaussian fitting procedure. This procedure allowed the robust and automatic identification of the peaks and their evolution along the reaction coordinate with no need for manual intervention. This method helped to attribute the peaks to the right species and gave the kinetic curves of those species directly. The isotopes ^{13}C and D were used to assist the assignment of the infrared peaks. From the analysis of ex situ $HCOO^-$* and CO_2 hydrogenation on Ru/Al_2O_3 and on Al_2O_3 surfaces, those kinetic curves of the resolved species revealed straightforwardly their reactivities during the reactions. In situ $HCOO^-$* formed from CO_2 hydrogenation was assigned thanks to the peak analysis of ex situ $HCOO^-$*, even though the reactivities of each adsorption structure were distinct from those of ex situ $HCOO^-$*. During CO_2 hydrogenation, in situ $HCOO^-$* adsorbed on the metal–support interface exhibited a high reactivity, similar to that during CO_2 conversion; in situ $HCOO^-$* adsorbed on Ru showed less reactivity; and in situ $HCOO^-$* adsorbed on Al_2O_3 was inactive. Bicarbonate also showed high reactivity, similar to that in CO_2 conversion. CO* showed distinctive properties during CO_2 hydrogenation, in that it was formed until the middle of the reaction and reduced afterward. These results from BEGF analysis are identical to those of our previous work by manual iteration of Gaussian fitting. This BEGF method is not only suitable for IR spectra but also universal for the deconvolution of overlapping spectra.

■ ASSOCIATED CONTENT

Supporting Information

The Supporting Information is available free of charge on the ACS Publications website at DOI: 10.1021/acs.jpcc.8b11105.

All of the figures mentioned in the main text, including HCOOH adsorption and hydrogenation on Al_2O_3; FT-IR transmittance of Na_2CO_3, $CaCO_3$, $KHCO_3$, and $NaHCO_3$; CO_2 adsorption and hydrogenation on Al_2O_3; the BEGF program (PDF)

■ AUTHOR INFORMATION

Corresponding Authors

*E-mail: kun.zhao@epfl.ch (K.Z.).
*E-mail: marco.calizzi@epfl.ch (M.C.).

ORCID

Kun Zhao: 0000-0002-7182-8089
Marco Calizzi: 0000-0001-5319-2657

Author Contributions

$^{\perp}$K.Z. and L.W. contributed equally to this work.

Notes

The authors declare no competing financial interest.

■ ACKNOWLEDGMENTS

SCCER HeE, which is financially supported by Innosuisse, the Swiss Innovation Agency, is gratefully acknowledged. K.Z. also gratefully thanks Daniel Auerbach for the full discussions and revisions of this work.

DOI: 10.1021/acs.jpcc.8b11105
J. Phys. Chem. C 2019, 123, 8785–8792

REFERENCES

(1) Wang, F.; He, S.; Chen, H.; Wang, B.; Zheng, L.; Wei, M.; Evans, D. G.; Duan, X. Active Site Dependent Reaction Mechanism over Ru/CeO_2 Catalyst toward CO_2 Methanation. *J. Am. Chem. Soc.* **2016**, *138*, 6298−6305.

(2) Sápi, A.; Halasi, G.; Kiss, J.; Dobó, D. G.; Juhász, K. L.; Kolcsár, V. J.; Ferencz, Z.; Vári, G.; Matolin, V.; Erdőhelyi, A.; et al. In Situ DRIFTS and NAP-XPS Exploration of the Complexity of CO_2 Hydrogenation over Size-Controlled Pt Nanoparticles Supported on Mesoporous NiO. *J. Phys. Chem. C* **2018**, *122*, 5553−5565.

(3) Martin, N. M.; Hemmingsson, F.; Wang, X.; Merte, L. R.; Hejral, U.; Gustafson, J.; Skoglundh, M.; Meira, D. M.; Dippel, A.-C.; Gutowski, O.; et al. Structure−Function Relationship during CO_2 Methanation over Rh/Al_2O_3 and Rh/SiO_2 Catalysts under Atmospheric Pressure Conditions. *Catal. Sci. Technol.* **2018**, *8*, 2686−2696.

(4) Xu, M.; Yao, S.; Rao, D.; Niu, Y.; Liu, N.; Peng, M.; Zhai, P.; Man, Y.; Zheng, L.; Wang, B.; et al. Insights into Interfacial Synergistic Catalysis over Ni@TiO_2−x Catalyst toward Water−Gas Shift Reaction. *J. Am. Chem. Soc.* **2018**, *140*, 11241−11251.

(5) Zhang, S. R.; Tang, Y.; Nguyen, L.; Zhao, Y. F.; Wu, Z.; Goh, T. W.; Liu, J. J. Y.; Li, Y. Y.; Zhu, T.; Huang, W. Y.; et al. Catalysis on Singly Dispersed Rh Atoms Anchored on An Inert Support. *ACS Catal.* **2018**, *8*, 110−121.

(6) Newton, M. A.; Ferri, D.; Smolentsev, G.; Marchionni, V.; Nachtegaal, M. Kinetic Studies of the Pt Carbonate-Mediated, Room-Temperature Oxidation of Carbon Monoxide by Oxygen over Pt/Al_2O_3 Using Combined, Time-Resolved XAFS, DRIFTS, and Mass Spectrometry. *J. Am. Chem. Soc.* **2016**, *138*, 13930−13940.

(7) Szanyi, J.; Kwak, J. H. Dissecting the Steps of CO_2 Reduction: 2. The Interaction of CO and CO_2 with Pd/γ-Al_2O_3: an In Situ FTIR Study. *Phys. Chem. Chem. Phys.* **2014**, *16*, 15126−15138.

(8) Taifan, W.; Boily, J.-F.; Baltrusaitis, J. Surface Chemistry of Carbon Dioxide Revisited. *Surf. Sci. Rep.* **2016**, *71*, 595−671.

(9) Marwood, M.; Doepper, R.; Renken, A. In-situ Surface and Gas Phase Analysis for Kinetic Studies under Transient Conditions the Catalytic Hydrogenation of CO_2. *Appl. Catal., A* **1997**, *151*, 223−246.

(10) Zheng, J.; Wang, C.; Chu, W.; Zhou, Y.; Köhler, K. CO_2 Methanation over Supported Ru/Al_2O_3 Catalysts: Mechanistic Studies by In Situ Infrared Spectroscopy. *ChemistrySelect* **2016**, *1*, 3197−3203.

(11) Miao, B.; Ma, S. S. K.; Wang, X.; Su, H.; Chan, S. H. Catalysis Mechanisms of CO_2 and CO Methanation. *Catal. Sci. Technol.* **2016**, *6*, 4048−4058.

(12) Chin, S. Y.; Williams, C. T.; Amiridis, M. D. FTIR Studies of CO Adsorption on Al_2O_3- and SiO_2-Supported Ru Catalysts. *J. Phys. Chem. B* **2006**, *110*, 871−882.

(13) Deb, K. An Introduction to Genetic Algorithms. *Sadhana* **1999**, *24*, 293−315.

(14) Zhao, K.; Wang, L.; Calizzi, M.; Moioli, E.; Zuttel, A. In Situ Control of the Adsorption Species in CO_2 Hydrogenation: Determination of Intermediates and Byproducts. *J. Phys. Chem. C* **2018**, *122*, 20888−20893.

(15) Shido, T.; Asakura, K.; Iwasawa, Y. Reactant-Promoted Reaction Mechanism for Catalytic Water-Gas Shift Reaction on MgO. *J. Catal.* **1990**, *122*, 55−67.

(16) Wilmshurst, J. K.; Bernstein, H. J. The Infrared Spectra of CH_4, CH_3D, CH_2D_2, CD_3H, and CD_4. *Can. J. Chem.* **1957**, *35*, 226−235.

(17) Garbarino, G.; Bellotti, D.; Finocchio, E.; Magistri, L.; Busca, G. Methanation of Carbon Dioxide on Ru/Al_2O_3: Catalytic Activity and Infrared Study. *Catal. Today* **2016**, *277*, 21−28.

(18) Hoffmann, F. M. Infrared Reflection-Absorption Spectroscopy of Adsorbed Molecules. *Surf. Sci. Rep.* **1983**, *3*, 107−192.

(19) Hadjiivanov, K. I.; Vayssilov, G. N. Characterization of Oxide Surfaces and Zeolites by Carbon Monoxide as an IR Probe Molecule. *Adv. Catal.* **2002**, *47*, 307−511.

DOI: 10.1021/acs.jpcc.8b11105
J. Phys. Chem. C 2019, 123, 8785−8792